Materials Advances

ROYAL SOCIETY OF CHEMISTRY

PAPER

View Article Online
View Journal

Cite this: DOI: 10.1039/d6ma00242k

Boron-fused pyrazolyl zinc salen as a self-powered ultra-sensitive sensor for picomolar nicotine detection in realistic smoke environments

Sasmita Dhala,†[a] Prakash Nayak,†[a] Indrajit Mondal,†[b] Chinmaya Sahoo,[b] Satyaprasad P. Senanayak *[bc] and Krishnan Venkatasubbaiah *[ac]

Received 19th February 2026,
Accepted 7th April 2026

DOI: 10.1039/d6ma00242k

rsc.li/materials-advances

Sensitive detection of nicotine is essential owing to its adverse effects on human health; in particular, nicotine is associated with increased risk of cardiovascular and respiratory disorders and multiple types of cancer. Although a large number of sensors for the detection of nicotine are known, the development of quick, easy and sensitive methods is in great demand. Herein, we report a tetra-coordinated boron-embedded zinc salen complex (**TPZBSA-Zn**) as a dual-mode sensor for the detection of nicotine. The complex exhibited a hypsochromic shift in fluorescence from green to blue upon the addition of nicotine. The observed luminescence shift is rationalized owing to the interaction between nicotine's pyridine nitrogen and the zinc center, as confirmed by NMR. Single crystal X-ray analysis revealed the binding mode of nicotine to the zinc–salen, which is responsible for the color change realized in fluorescence studies. We further developed a highly sensitive nicotine detection device based on conductivity modulation arising from Zn–N coordination, capable of detecting nicotine in both the vapor and liquid phases at concentrations as low as 1 pM (10^{-12} M). The device exhibited exceptional responsiveness and reliability, demonstrating superior performance even under real cigarette and bidi smoke exposure in indoor settings.

Introduction

The usage of tobacco through cigarette smoking is widespread throughout the world and is regarded as an addiction with serious global health consequences. The development of several cancers, most notably lung cancer, as well as respiratory and cardiovascular disorders, has been related to prolonged and excessive inhalation of cigarette smoke.[1–4] The addictive nature of tobacco smoking is mainly attributed to the presence of nicotine. Among the different organic moieties and gases present in cigarette smoke, nicotine is found to be one of the most harmful constituents. Nicotine is highly toxic and can be fatal to an adult at a dosage of 40–60 mg. More than 5 million deaths per year are attributed to tobacco/nicotine intake.[5,6] Nicotine is also introduced into the body of nonsmokers *via* second-hand or passive smoking, which is also harmful, causing health issues and deaths.[7–11] Passengers and cabin crew of aircraft and workers of private and public companies in a closed environment have faced severe problems owing to passive smoking. Moreover, in such indoor settings, smoking is a well-known fire hazard. Hence, it is important to monitor the air quality in public and private places, especially the level of nicotine in the air.

Detection of nicotine has been studied mostly *via* electrochemical methods; for instance, multi-walled carbon nanotubes, nitrogen-doped graphene, graphene composites, graphene oxide-supported gold nanoparticles, boron-doped diamond, and activated glassy carbon cerium nanoparticles have been applied for the electrochemical detection method.[12–22] Spectrophotometry, chromatography, reverse HPLC, and colorimetric methods have also been used for the detection of nicotine.[23–35] However, most of the methods require sophisticated instrumentation, complicated methods and high cost. Therefore, it is important to develop highly selective, convenient yet sensitive and rapid nicotine detection methods. In this regard, the fluorescence-based technique has emerged as a powerful approach for the detection of nicotine due to its high sensitivity, operational simplicity, rapid response and real-time monitoring. Moreover, fluorescent probes typically exhibit very low detection limits as

[a] *School of Chemical Sciences, National Institute of Science Education and Research (NISER), an OCC of Homi Bhabha National Institute, Bhubaneswar, 752050, Odisha, India. E-mail: krishv@niser.ac.in*
[b] *School of Physical Sciences, National Institute of Science Education and Research (NISER), an OCC of Homi Bhabha National Institute, Bhubaneswar, 752050, Odisha, India. E-mail: satyaprasad@niser.ac.in*
[c] *Centre for Interdisciplinary Sciences (CIS), National Institute of Science Education and Research, Bhubaneswar, Odisha, 752050, India*
† Equally contributed.

well as a high signal-to-noise ratio. This makes them well-suited for detecting trace-level analytes.

Tetra-coordinated boron-based fluorophores,[36–42] especially B–N coordinated fluorophores, have gained attention owing to their stability and tunable optical properties. B–N coordinated fluorophores display remarkable properties, such as oxygen sensing, photochromism, *etc.*[43–59] The incorporation of boron atoms into a polyhydrocarbon framework not only provides structural rigidity by suppressing the non-radiative decay pathways, but also modulates the electronic distribution, thereby increasing fluorescence efficiency and improving response to the environment. Recently, we reported the synthesis of monomers and dimers of B–N coordinated phenanthroimidazoles and tri-aryl pyrazoles and studied their optical properties.[46,48–60] We further utilized B–N coordinated phenanthroimidazoles to make zinc(II) salen and utilized them for the transformation of carbon dioxide and epoxides/aziridines to cyclic carbonates/oxazolidinones, respectively, under mild reaction conditions and also for lanthanoid discrimination.[61–63] Taking advantage of the strong emission characteristics, tunable photophysical properties and remarkable photostability of the B–N coordinated compounds with the chelating capability of salen ligands, here, we report a boron-functionalized pyrazole-based Zn–salen complex for the detection of nicotine. To our delight, our complex exhibited two independent modes of detection, namely fluorometric and conductivity modes. Using the fluorometric method, it was possible to detect up to 1.4 μM of nicotine concentration in the solution state, whereas with the conductometric technique method the nicotine can be detected at the picomolar concentration both in the solution and vapor phase.

Results and discussion

Synthesis and characterization

The synthetic procedure used to obtain boron-fused pyrazole imine ligand **TPZBSA** is shown in Scheme 1. Compound **TPZB** was synthesized according to the literature reported methods.[60] Synthesis of the desired ligand **TPZBSA** was realized in good yield (88%) by simple condensation of *trans*-1,2-diaminocyclohexane with two equivalents of **TPZB** in dry methanol. The targeted Zn(II) complex **TPZBSA-Zn** was prepared in 84% yield by reacting **TPZBSA** and zinc acetate in a 1 : 1 ratio in CH_3OH/CH_2Cl_2 for 12 hours under reflux conditions. **TPZBSA** and **TPZBSA-Zn** were analysed using multi-nuclear NMR spectroscopy and HRMS. The absence of a phenolic –OH peak at 13.39 ppm of **TPZBSA** and the shift (up-field) of two protons of cyclohexyl from 3.41 ppm in **TPZBSA** to 3.23 ppm in **TPZBSA-Zn** establishes the formation of a Zn^{2+} compound. To our excitement, X-ray quality crystals of **TPZBSA-Zn** were grown in the DMSO/MeOH solvent system. Complex **TPZBSA-Zn** crystallizes in a monoclinic $P2_1/c$ space group. The crystal structure reveals a distorted square pyramidal five-coordinate geometry around the zinc atom (Fig. 1). The axial position is coordinated with a DMSO solvent molecule with a bond length of 2.029 Å. The zinc atom deviates by 0.447 Å with respect to the N_2O_2 plane of the salen motif. The zinc–oxygen/nitrogen bond angles and distances observed for complex **TPZBSA-Zn** are in agreement with literature reported Zn^{2+} salen compounds.[61–66] Selected bond angles and bond lengths are listed in Table S3. The bond angle investigation reveals that two boron centers attain a distorted tetrahedral geometry. At the B1 center, the C–B1–C bond angles range from 113.0° to 115.2° and the C–B1–N bond angles range from 94.6° to 112.4°. Similarly, at the B2 center, the C–B2–C bond angles range from 110.3° to 114.7° and the C–B2–N bond angles range from 94.6° to 109.5°.

Photophysical properties

After successfully characterizing the **TPZBSA-Zn** complex, we studied its photophysical properties in $CHCl_3$. Complex **TPZBSA-Zn** displayed a red-shifted absorption maximum at 375 nm in comparison to ligand **TPZBSA**, which has an absorption maximum at 327 nm in $CHCl_3$. Similarly, complex **TPZBSA-Zn** showed an emission maximum at 484 nm in comparison to ligand **TPZBSA**, which showed an emission maximum at 457 nm.

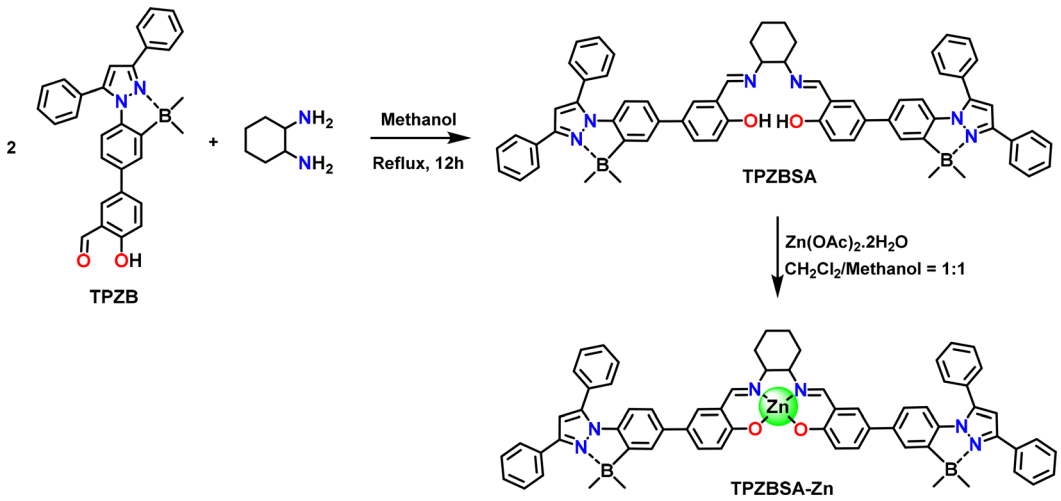

Scheme 1 Synthesis of zinc complex **TPZBSA-Zn**.

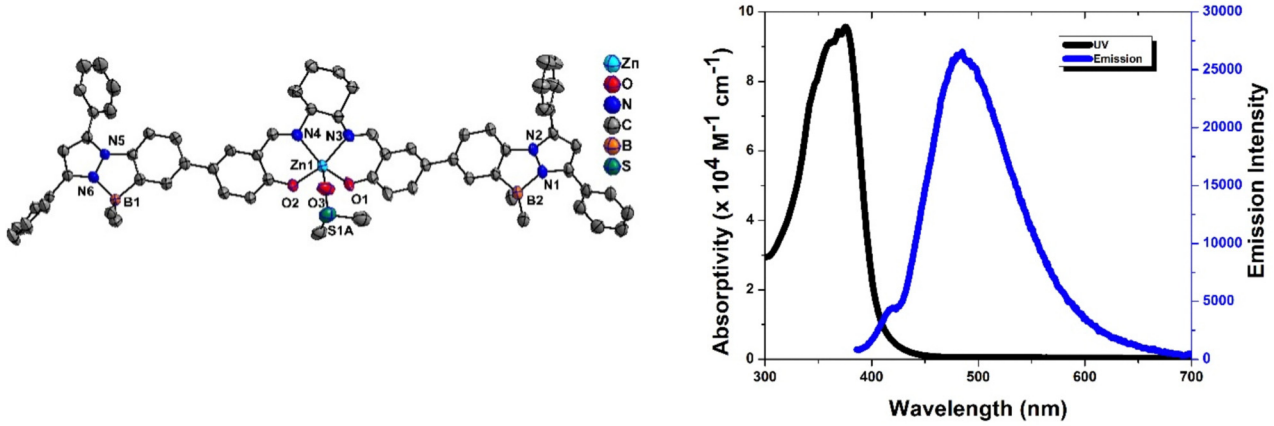

Fig. 1 (Left) Molecular structure of **TPZBSA-Zn**-DMSO. (Right) Absorbance and emission spectra of complex **TPZBSA-Zn** in $CHCl_3$ at 1×10^{-5} M concentration.

Complex **TPZBSA-Zn** showed an intense emission and better quantum yield (Φ_F = 13.3%) compared to the ligand. **TPZBSA-Zn** exhibited mechanofluorochromic properties. As shown in Fig. 2, it was observed that the prepared powder of **TPZBSA-Zn** emitted a bright blue color under UV irradiation. The solid-state emission band of **TPZBSA-Zn** in the as-synthesised powder was found at 474 nm and shifted to a longer wavelength of 535 nm after grinding using a mortar and pestle. This suggests that the grinding treatment resulted in a spectral bathochromic shift of 61 nm for complex **TPZBSA-Zn**. Furthermore, the prepared **TPZBSA-Zn** showed 4.3% quantum yield in the solid state, which was reduced to 1.1% upon grinding. When we exposed the ground powder of **TPZBSA-Zn** to dichloromethane vapor, the luminescence recovered to cyan color with emission maximum at 502 nm, close to that of the original powder. It should be noted that repeated grinding–fuming cycles of **TPZBSA-Zn** resulted in interchange of the luminescence spectra with a 32 nm difference in the emission maxima (Fig. 2).

To further explore the mechanofluorochromic properties of **TPZBSA-Zn**, X-ray diffraction (XRD) measurements for the powdered sample were analysed. As given in Fig. 2e, the freshly synthesized powder of **TPZBSA-Zn** showed many strong and sharp peaks, suggesting that the well-defined microcrystalline-like structure prevails in the freshly prepared sample. On the other hand, the ground powder showed very weak or no noticeable diffraction peaks, indicating the amorphous nature in this state. Upon fumigating with DCM, the crystalline nature was restored to a certain extent with few sharp and diffused peaks. To further investigate the mechano-luminescence properties, the crystal structure of complex **TPZBSA-Zn** was investigated.

According to previous reports, weak intermolecular interactions play an important role in mechanoluminescence.[67–71] Strong intermolecular interactions, like π–π stacking, were not detected in **TPZBSA-Zn**, and only multiple short interatomic contacts were found within the crystals. As shown in Fig. 2f and g, complex **TPZBSA-Zn** has C–H···π interactions. The emission color change on grinding is possibly due to changes in these intermolecular interactions between molecules. From the above studies, it is clear that the mechanoluminescence of **TPZBSA-Zn** is due to changes in both conformational and intermolecular interactions.

As the crystalline form has C–H···π interactions, they help to restrict the torsional motion of the rings which help to release the excited state energy by a radiative decay process; hence, the crystalline form is more emissive. However, in the amorphous phase the weak interactions are absent; hence, energy decay by non-radiative decay becomes prominent and thus the quantum yield is low in the ground sample. To evaluate the stability of the probe, the fluorescence emission of **TPZBSA-Zn** was monitored over a period of 60 minutes at regular intervals of 5–10 minutes, which showed negligible changes in emission intensity, confirming its good photostability over prolonged durations (Fig. S2). Additionally, the thermal stability was examined by recording the emission spectra over a temperature range of 25 °C to 55 °C. The absence of significant changes in the emission spectra indicates that the probe retains its photophysical properties, depicting good kinetic stability (Fig. S3).

Nicotine sensing

We took advantage of the Lewis acidic nature of the zinc center to detect nicotine. The fluorescence spectra of **TPZBSA-Zn** were recorded upon excitation at 374 nm with the addition of different amounts of nicotine. Sequential addition of nicotine (0–40 equiv.) to **TPZBSA-Zn** resulted in a gradual decrease of the fluorescence band at 484 nm with the simultaneous appearance of an emission in the range of 387 nm to 413 nm (Fig. 3). The fluorescence lifetime of **TPZBSA-Zn** measured in the absence and presence of nicotine was found to be consistent (life time for **TPZBSA-Zn** in $CHCl_3$ is 1.60 ns; life time for **TPZBSA-Zn** + 20 equivalent of nicotine in $CHCl_3$ is 1.67 ns) suggesting that quenching follows a static-mechanism. The observed lifetime measurements reveal that a ground-state complex is formed between **TPZBSA-Zn** and nicotine. The detection limit of nicotine using **TPZBSA-Zn** was determined to be 1.4 μM, which motivated us to make a device using our complex for the detection of nicotine in the solution as well as in the solid

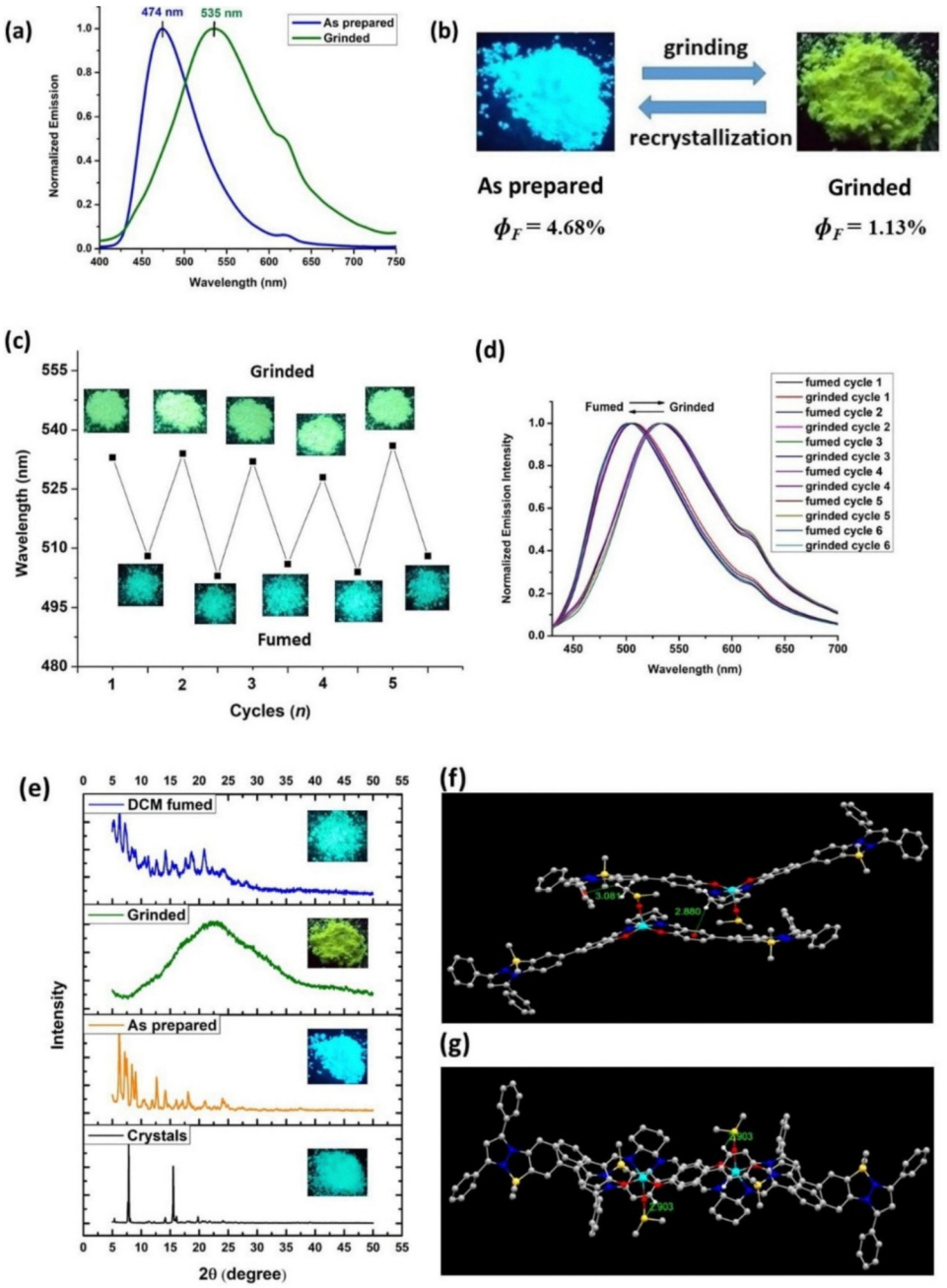

Fig. 2 (a) Normalized fluorescence spectra of **TPZBSA-Zn** and **TPZSA-Zn** in different solid-states: as-prepared and grinding, λ_{ex} = 340 nm; (b) photographs of **TPZBSA-Zn** and **TPZSA-Zn** color changes under grinding and recrystallization; (c) reversible switching emission of complex **TPZBSA-Zn** by repeated grinding–fuming cycles; (d) emission spectra of complex **TPZBSA-Zn** after repeated grinding–fuming cycles; (e) PXRD patterns of complex **TPZBSA-Zn** in different solid states: as-prepared, grinding and DCM fuming. Inset: photographs of complex **TPZBSA-Zn** in different solid states (as prepared, grinded and fumed) under a hand-held UV-lamp; (f) CH$\cdots\pi$ interactions in complex **TPZBSA-Zn**; (g) H-bonding interactions in complex **TPZBSA-Zn**.

state, which will be discussed *vide infra*. In order to investigate the interaction between **TPZBSA-Zn** and nicotine, we performed NMR studies and single-crystal X-ray diffraction analysis. The ^{1}H NMR of nicotine with **TPZBSA-Zn** showed a shift in $CDCl_3$ for the pyridine–H, which reveals the complexation of pyridine with the zinc center in the solution state as observed in other zinc complexes.[61–66] To further support this observation, we grew single crystals of **TPZBSA-Zn**–nicotine in methanol/DMSO solution. Single crystal-XRD analysis showed the formation of a 1 : 1 adduct, in which the pyridine nitrogen of nicotine binds with the zinc atom of **TPZBSA-Zn** to form a penta-coordinated zinc complex. The bond angles and bond lengths are reminiscent of the literature-reported values of similar compounds (Table S4).[61–66] A paper strip of compound **TPZBSA-Zn** was

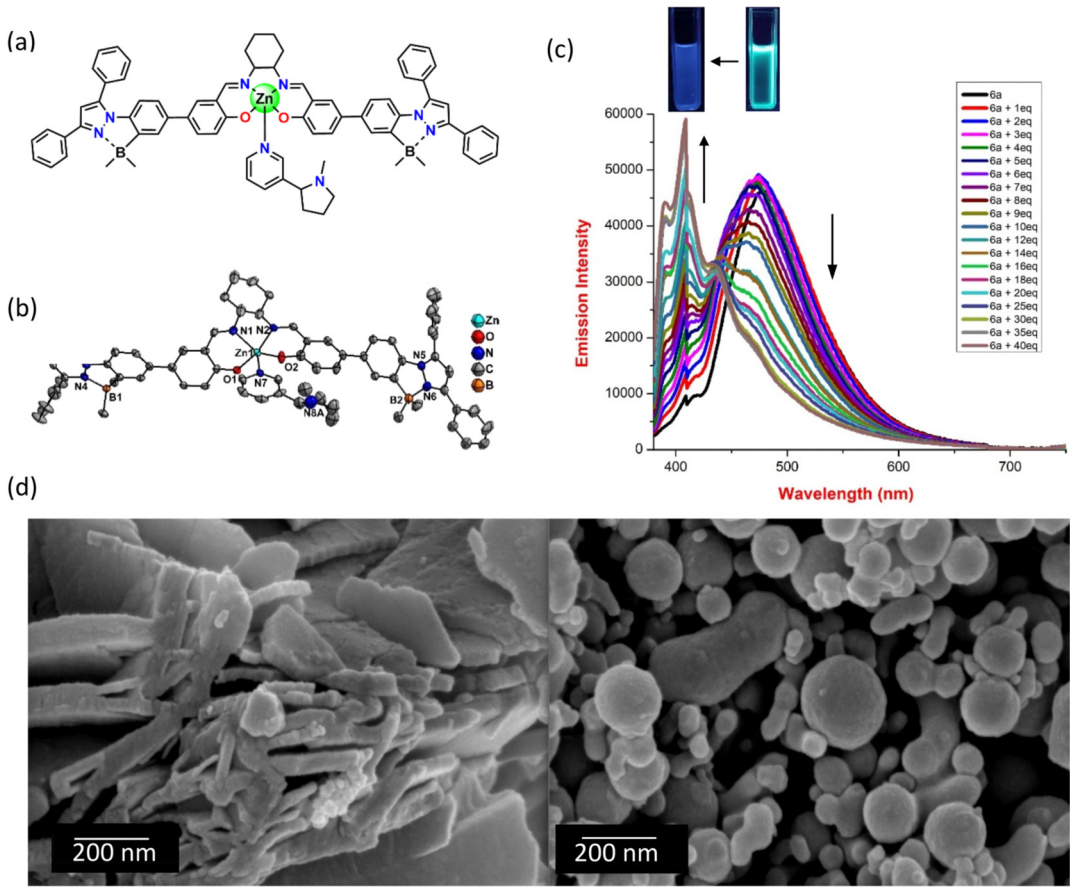

Fig. 3 (a) Structure of **TPZBSA-Zn**–nicotine. (b) Molecular structure of **TPZBSA-Zn**–nicotine (hydrogen atoms and disordered cyclohexyl were removed for clarity). (c) Titration curve for **TPZBSA-Zn** (1×10^{-5} M) with increasing equivalents of nicotine in $CHCl_3$ (inset: before and after addition of nicotine under a hand-held UV lamp). (d) SEM images of **TPZBSA-Zn** (left) and nicotine-coordinated **TPZBSA-Zn** (right).

prepared by immersing Whatman filter paper in a $CHCl_3$ solution of compound **TPZBSA-Zn** followed by drying in open air. A solution of nicotine in $CHCl_3$ was used to make encryption 'NISER'. A change in fluorescence color was realized in the encrypted place, which indicates the usefulness of the paper strip for the detection of nicotine (Fig. S7). The surface morphology of **TPZBSA-Zn** and nicotine-coordinated **TPZBSA-Zn** was analyzed using SEM. The **TPZBSA-Zn** exhibited a lamellar morphology (Fig. 3d-left), whereas the nicotine-coordinated **TPZBSA-Zn** showed a spherical morphology (Fig. 3d-right). To assess the selectivity of the probe, we examined its response towards nicotine in the presence of various primary (1°) and secondary (2°) amines as well as pyridine (40 equivalents). Notably, only nicotine and pyridine showed a significant hypsochromic shift in the fluorescence, indicating selective interaction. This behaviour can be attributed to coordination through the pyridine nitrogen moiety, thereby enhancing the selectivity of the probe toward nicotine over other amines (Fig. S4).

To explore the nicotine sensing potential of the synthesized material going beyond conventional fluorescence-based detection, we fabricated two-terminal devices. For the device fabrication, patterned Au-electrodes were prepared *via* thermal evaporation on which the **TPZBSA-Zn** complex was spin-coated (schematic in Fig. 4a, details in the method section). Nicotine was systematically diluted from 10^{-12} M to 0.1 M, and a controlled volume ($\sim$20 μl) of each concentration was drop-casted onto the device surface (Fig. S10). Conductivity is estimated in the low voltage regime from a linear fit to the *I–V* characteristics. The pristine **TPZBSA-Zn** complex exhibited an initial conductivity of (465 ± 11) μS cm^{-1}, which sharply decreased to (400 ± 30) μS cm^{-1} even upon exposure to an extremely low nicotine concentration of 10^{-12} M, demonstrating its remarkable picomolar level sensitivity. As the nicotine concentration increased further, the conductivity continued to drop progressively, reaching as low as (10 ± 2) μS cm^{-1} at 0.1 M, over four orders of magnitude lower than that of the unexposed device (Fig. S11). Channel current variation with nicotine concentration is depicted in Fig. 4b, and the corresponding increase in device resistance is shown in Fig. 4c. The relative conductivity varied by nearly one order of magnitude across the sensing window (10^{-12}–10^{-2} M), as shown in Fig. 4d. A clear morphological change is observed when the devices were exposed to higher concentration (0.01 M) of liquid phase nicotine, which renders the device conductivity irreversible (Fig. S12). Notably, these self-powered devices exhibit a measurable current output (13 nA) even at zero applied bias, indicating autonomous device operation driven by intrinsic charge separation. In the self-

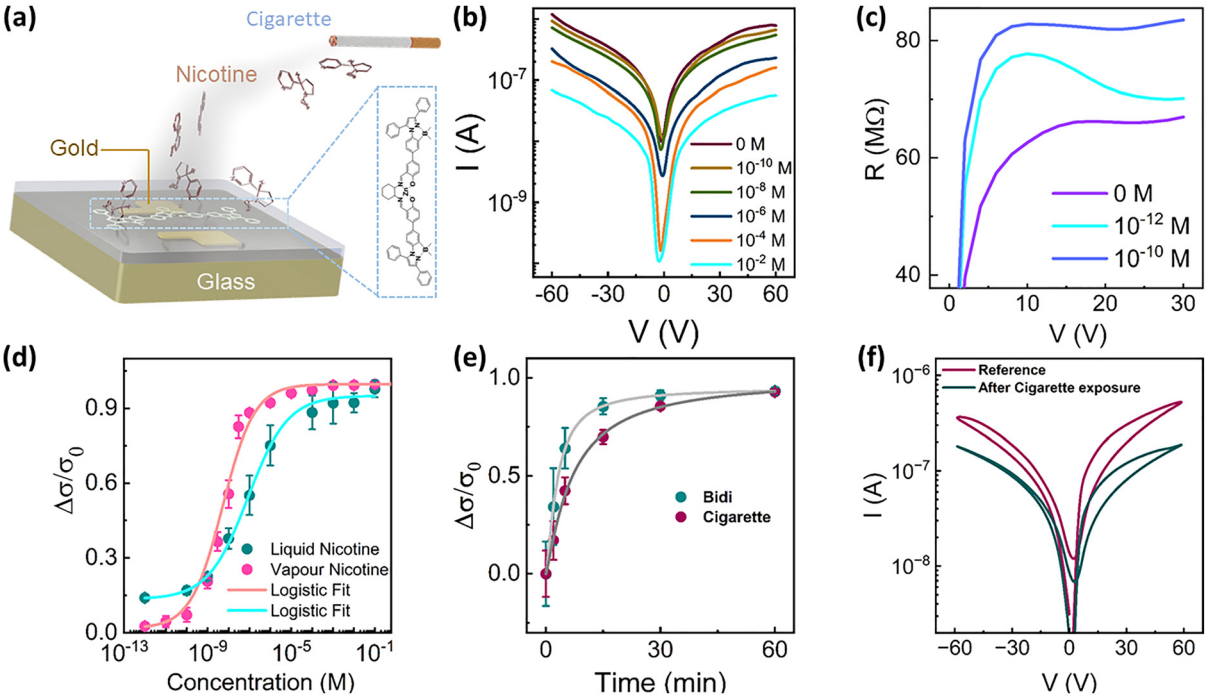

Fig. 4 (a) Schematic diagram of the device architecture illustrating nicotine sensing. (b) *I*–*V* characteristic of the device upon liquid-nicotine exposure of different concentrations. (c) Variation of the resistance of the device upon nicotine exposure of different concentrations in the liquid phase. (d) Relative conductivity of the device on nicotine exposure of different concentrations in the vapor phase for 60 minutes. (e) Relative conductivity of the device with time upon bidi and cigarette exposure. (f) *I*–*V* characteristic curves before and after exposure to cigarettes.

powered mode these nicotine sensors exhibit a current of ~7 nA even with 1 pM concentration. These conductometric trends highlight the exceptional interaction between nicotine molecules and the **TPZBSA-Zn** complex, leading to significant modulation of charge transport pathways within the film. The zinc-based organometallic complex interacts with nicotine through a dative bond formation between the Zn atom and the nitrogen of the pyridine ring (Fig. 3a), resulting in the formation of a ground-state charge–transfer complex between the Lewis acidic Zn centre and the Lewis basic pyridine nitrogen of nicotine. This interaction perturbs the electronic structure of **TPZBSA-Zn**, modifying the conjugated π-system for efficient charge transport.[72] The static quenching observed in lifetime measurements further confirms that a non-emissive, electronically altered complex forms in the ground state. This interaction leads to a blue shift in the emission spectra with increasing nicotine concentration, indicating an increase in the effective bandgap of the nicotine–**TPZBSA-Zn** complex which possibly decreases the overall electrical conductivity. We also performed similar measurements by utilizing vapour phase nicotine obtained by heating nicotine solutions at 70 °C and inducing reaction between nicotine vapours and the **TPZBSA-Zn** complex, which exhibited similar conductivity trends (Fig. 4d).

To obtain a detailed understanding of the conductometric trends and reliability of the sensing device, we fitted the conductivity response $\left(\frac{\Delta\sigma}{\sigma}\right)$ as a function of nicotine concentration. The conductivity response followed a sigmoidal (S-shaped) trend (Fig. 4d and Fig. S13), typical of systems limited by binding saturation or diffusion kinetics. This behaviour was successfully modelled using a logistic function (details in SI section S6), enabling quantitative comparison of device response and insights into the underlying interaction dynamics. From this modelling, we obtain three specific parameters: (a) dynamic range which depicts the concentration range over which the sensor is sensitive, (b) inflection point which corresponds to the operational sensitivity threshold, (c) slope parameter which depicts a comparative sensitivity to different samples at the lowest sensing concentration. For liquid nicotine exposure (Fig. 4d and Fig. S11), the logistic model yielded a dynamic range of 0.8, indicating that the sensor is effectively able to sense in 80% of the concentration range between the initial and final conductivity states. The midpoint concentration $(6 \pm 4) \times 10^{-8}$ M corresponded to the inflection point where the response rate of the sensor is maximal, defining the operational sensitivity threshold. The low slope factor (k = 0.3) indicated a gradual, well-regulated transition, demonstrating predictable sensing behaviour over a broad concentration range. In contrast, logistic analysis of vapour-phase nicotine sensing (Fig. 4d and Fig. S13) revealed enhanced device performance, with an expanded dynamic range of 0.98 and a steeper slope parameter (k = 0.5), indicating more rapid and efficient molecular interaction with the sensing layer. The lower midpoint concentration $((5.2 \pm 2.1) \times 10^{-9}$ M) suggests higher sensitivity under vapour exposure relative to liquid exposure. Collectively, these parameters confirm that nicotine vapour induces a faster and more pronounced change in conductivity, offering improved sensitivity and dynamic resolution suitable for real-environment sensing.

To assess real-world usability, we utilized cigarette and bidi (a local form of tobacco) smoke, and exposure was carried out in a sealed 100 mL chamber (Fig. 4e). Both smoke types produced conductivity suppression by approximately 20% and 30%, respectively, after 2 minutes of exposure, consistent with pristine nicotine results in liquid and vapor states. Interestingly logistic fitting of both these tobacco sources exhibited sensitivity values between that of the liquid nicotine and vapor nicotine. Notably, the slope factor indicates that bidi owing to its larger concentration of nicotine, exhibits a stronger sensitivity in comparison to cigarettes. This level of sensitivity encouraged us to validate our sensor's deployment potential, which involved a direct human smoking trial inside a 45 ft^3 controlled chamber, a volume comparable to that of a standard aircraft lavatory. The nicotine-sensing device was positioned approximately 15 cm from the volunteer, who exhaled cigarette smoke directly toward the sensor. Before introducing smoke, a control experiment was performed in which the participant gently blew plain air toward the device to rule out any artefacts from temperature, humidity changes, or airflow disturbance. The pristine device exhibited an initial conductivity of 264 $\pm$ 4 $\mu S\ cm^{-1}$. After five controlled air blows, the conductivity showed only a minor reduction to 250 $\pm$ 3 $\mu S\ cm^{-1}$, corresponding to roughly a 5% change, confirming that environmental perturbation alone does not significantly affect the sensing response. In stark contrast, when exposed to five exhalations of cigarette smoke, the conductivity dropped sharply to 175 $\pm$ 3 $\mu S\ cm^{-1}$, representing an approximate 30% decrease (Fig. 4f and Fig. S14). Moreover, control experiments with human subject blows without smoking exhibited insignificant variation in conductivity, indicating that environmental and humidity-driven artefacts do not affect these sensors. This level of performance highlights the applicability of our device in real smoke sensor applications & highlights the strong affinity and rapid interaction of nicotine with the **TPZBSA-Zn** sensing layer. We also checked the reversibility of the sensor to ambient nicotine exposure and realized significant reversibility (Fig. S15) and observed reasonable reversibility for multiple cycles of detection. These findings underscore the device's potential for deployment in enclosed public spaces for exposure monitoring, smoking compliance enforcement, and real-time air-quality assessment. A comparison of previously reported nicotine-sensing methods with the present **TPZBSA-Zn** system is presented in Table S5. Notably, the present system offers several advantages, namely dual mode of detection (fluorescence and conductometric detection), a detection limit at the picomolar level and the ability to sense nicotine in both liquid and vapor phases. Furthermore, the fabricated device responds to real cigarette and local tobacco smoke, highlighting its practical applicability for environmental nicotine monitoring.

Conclusions

In conclusion, we have successfully developed a B–N coordinated triaryl pyrazolyl zinc–salen complex **TPZBSA-Zn** as a dual-mode sensor for nicotine detection. The complex **TPZBSA-Zn** exhibits unique photophysical properties, including mechanochromism and a remarkable fluorescence shift upon nicotine binding, driven by coordination of the pyridine nitrogen of the nicotine to the zinc centre. The binding mode of nicotine with zinc–salen **TPZBSA-Zn** was confirmed using ^1H NMR and single-crystal X-ray analysis. Furthermore, we fabricated devices using **TPZBSA-Zn** and studied its relative change of conductivity with different concentrations of nicotine in the solution and in the vapor phase, which suggests that our device can suitably detect nicotine concentration as low as 1 picomolar in both the vapor and liquid state. The system also effectively responded to nicotine from real sources such as cigarette smoke from human subjects in closed chambers emulating real-time environmental application. These findings establish **TPZBSA-Zn** as a promising candidate for low-cost, portable, and real-time nicotine monitoring technologies applicable in environmental and health surveillance.

Author contributions

S. D., P. N. and I. M. contributed equally to this work. K. V. and S. P. S. conceptualized the study and provided overall supervision. S. D. and P. N. performed the synthesis, structural elucidation, and photophysical sensing behaviour of the nicotine-coordinated Zn complex. I. M. and C. S. made the nicotine sensing device, and performed *I–V* measurement, data analysis and all experiments related to conductometric nicotine sensing.

Conflicts of interest

There are no conflicts to declare.

Data availability

The data that support the findings of this study are available in the supplementary information (SI). Supplementary information contains synthesis, characterization, photophysical studies of complex along with nicotine detection, NMR titration studies, crystallographic data and device fabrication methods. See DOI: https://doi.org/10.1039/d6ma00242k.

CCDC 2519213 and 2519214 contain the supplementary crystallographic data for this paper.[73a,b]

Acknowledgements

We acknowledge funding support from the Department of Atomic Energy (DAE-RIN 4001, DAE-RIN-4002, and DAE-RNI-4011) and the Science and Engineering Research Board (SERB) (CRG/2023/000085 and IPA/2021/00096) for financial support. We thank Dr Rupayan Biswas for the help he provided in measuring the cigarette smoke. S. D., P. N. and I. M. thank NISER for fellowships.

References

1 A. H. Weinberger, M. Gbedemah, M. M. Wall, D. S. Hasin, M. J. Zvolensky and R. D. Goodwin, *Addiction*, 2018, **113**, 719–728.
2 K. Bjartveit and A. Tverdal, *Tob. Control*, 2005, **14**, 315.
3 F. Musso, F. Bettermann, G. Vucurevic, P. Stoeter, A. Konrad and G. Winterer, *Psychopharmacology*, 2007, **191**, 159–169.
4 R. N. Proctor, *Tob. Control*, 2012, **21**, 87.
5 B. Le Foll, M. E. Piper, C. D. Fowler, S. Tonstad, L. Bierut, L. Lu, P. Jha and W. D. Hall, *Nat. Rev. Dis. Prim.*, 2022, **8**, 19.
6 R. West, *Psychol. Health*, 2017, **32**, 1018–1036.
7 M. H. Dehghani, P. Bashardoust, D. Nayeri, M. Rezvani Ghalhari, N. B. Yazdi, F. Jajarmi, R. R. Karri and N. M. Mubarak, in *Health Effects of Indoor Air Pollution*, ed. M. H. Dehghani, R. R. Karri, T. Vera and S. K. M. Hassan, Academic Press, 2024, pp. 167–189.
8 L. S. Flor, J. A. Anderson, N. Ahmad, A. Aravkin, S. Carr, X. Dai, G. F. Gil, S. I. Hay, M. J. Malloy, S. A. McLaughlin, E. C. Mullany, C. J. L. Murray, E. M. O'Connell, C. Okereke, R. J. D. Sorensen, J. Whisnant, P. Zheng and E. Gakidou, *Nat. Med.*, 2024, **30**, 149–167.
9 Y. Kawasaki, Y.-S. Li, Y. Ootsuyama, K. Fujisawa, H. Omori, A. Onoue, K. Kubota, T. Yoshino, Y. Nonami, M. Yoshida, H. Yamato and K. Kawai, *J. Clin. Biochem. Nutr.*, 2023, **72**, 242–247.
10 N. Ramírez, M. Z. Özel, A. C. Lewis, R. M. Marcé, F. Borrull and J. F. Hamilton, *Environ. Int.*, 2014, **71**, 139–147.
11 S.-Q. Wang, L.-J. Bao, T.-Y. Li and E. Y. Zeng, *J. Hazard. Mater.*, 2024, **480**, 136446.
12 Y. Chen, Y. Tang, P. Li, Y. Wang, Y. Zhuang, S. Sun, D. Wang and W. Wei, *Anal. Chim. Acta*, 2023, **1278**, 341739.
13 Z. O. Erdogan and H. Balci, *Spectrochim. Acta, Part A*, 2023, **285**, 121853.
14 A. M. Fekry, S. M. Azab, M. Shehata and M. A. Ameer, *RSC Adv.*, 2015, **5**, 51662–51671.
15 S. H. Hashemi and F. Keykha, *Anal. Methods*, 2019, **11**, 5405–5412.
16 Z. Huang, Z. Li, L. Xu, C. Wei, C. Zhu, H. Deng, H. Peng, X. Xia and W. Chen, *Anal. Chem.*, 2020, **92**, 11438–11443.
17 R. Jerome and A. K. Sundramoorthy, *Anal. Chim. Acta*, 2020, **1132**, 110–120.
18 Y. Jing, S. Ning, Y. Guan, M. Cao, J. Li, L. Zhu, Q. Zhang, C. Cheng and Y. Deng, *Front. Chem.*, 2020, **8**, 593070.
19 A. Mirani, E. Kianfar, L. Maleknia and M. Javanbakht, *Case Stud. Chem. Environ. Eng.*, 2024, **9**, 100753.
20 J. Rajendran, A. N. Reshetilov and A. K. Sundramoorthy, *Mater. Adv.*, 2021, **2**, 3336–3345.
21 T. I. Sebokolodi, D. S. Sipuka, C. Muzenda, O. V. Nkwachukwu, D. Nkosi and O. A. Arotiba, *Chemosphere*, 2022, **303**, 134961.
22 G. Sridharan, K. L. Babu, D. Ganapathy, R. Atchudan, S. Arya and A. K. Sundramoorthy, *Crystals*, 2023, **13**, 589.
23 K. R. Tambwekar, R. B. Kakariya and S. Garg, *J. Pharm. Biomed. Anal.*, 2003, **32**, 441–450.
24 X.-Y. Tao, Y. Zhang, Y. Zhou, Z.-F. Liu and X.-S. Feng, *Crit. Rev. Anal. Chem.*, 2023, **53**, 1209–1238.
25 J. Adamson, X. Li, H. Cui, D. Thorne, F. Xie and M. D. Gaca, *Appl In Vitro Toxicol.*, 2017, **3**, 14–27.
26 J. Aszyk, P. B. Kubica, A. Kot-Wasik, J. Namie≈blnik and A. Wasik, *J. Chromatogr. A*, 2017, **1519**, 45–54.
27 J. M. El-Khoury and S. Wang, *Bioanalysis*, 2014, **6**, 2171–2183.
28 M. Famele, J. Palmisani, C. Ferranti, C. Abenavoli, L. Palleschi, R. Mancinelli, R. M. Fidente, G. de Gennaro and R. Draisci, *J. Sep. Sci.*, 2017, **40**, 1049–1056.
29 M. A. Kaisar, R. R. Kallem, R. K. Sajja, A. E. Sifat and L. Cucullo, *BMC Neurosci.*, 2017, **18**, 71.
30 T. Taghavi, M. Novalen, C. Lerman, T. P. George and R. F. Tyndale, *Cancer Epidemiol., Biomarkers Prev.*, 2018, **27**, 882–891.
31 J. Yang, S. G. Carmella and S. S. Hecht, *J. Chromatogr. B: Anal. Technol. Biomed. Life Sci.*, 2017, **1044–1045**, 127–131.
32 T. Leelasree, S. Goel and H. Aggarwal, *ACS Appl. Nano Mater.*, 2022, **5**, 16753–16759.
33 D. Rani, K. K. Bhasin and M. Singh, *ACS Mater. Lett.*, 2020, **2**, 9–14.
34 G. R. Deviprasad and F. D'Souza, *Chem. Commun.*, 2000, 1915–1916.
35 E. C. Escudero-Adán, J. Benet-Buchholz and A. W. Kleij, *Inorg. Chem.*, 2008, **47**, 4256–4263.
36 M. Hirai, N. Tanaka, M. Sakai and S. Yamaguchi, *Chem. Rev.*, 2019, **119**, 8291.
37 S. K. Mellerup and S. Wang, *Chem. Soc. Rev.*, 2019, **48**, 3537.
38 Q. Xia, J. Zhang, X. Chen, C. Cheng, D. Chu, X. Tang, H. Li and Y. Cui, *Coord. Chem. Rev.*, 2021, **435**, 213783.
39 J. Han, Y. Chen, N. Li, Z. Huang and C. Yang, *Aggregate*, 2022, **3**, e182.
40 S. Bellinger, M. Hatamimoslehabadi, R. E. Borg, J. La, P. Catsoulis, F. Mithila, C. Yelleswarapu and J. Rochford, *Chem. Commun.*, 2018, **54**, 6352.
41 P. Li, H. Chan, S.-L. Lai, M. Ng, M.-Y. Chan and V. W.-W. Yam, *Angew. Chem., Int. Ed.*, 2019, **58**, 9088.
42 A. Wakamiya, T. Taniguchi and S. Yamaguchi, *Angew. Chem., Int. Ed.*, 2006, **45**, 3170–3173.
43 S. Mukherjee and P. Thilagar, *J. Mater. Chem. C*, 2016, **4**, 2647–2662.
44 Z. Feng, Y. Yu, X. Yang, Y. Sun, D. Zhong, X. Deng, G. Zhou and Z. Wu, *J. Mater. Chem. C*, 2021, **9**, 12650–12660.
45 J. Full, S. P. Panchal, J. Götz, A.-M. Krause and A. Nowak-Król, *Angew. Chem., Int. Ed.*, 2021, **60**, 4350–4357.
46 V. Mukundam, S. Sa, A. Kumari, R. Das and K. Venkatasubbaiah, *J. Mater. Chem. C*, 2019, **7**, 12725–12737.
47 A. C. Murali, P. Nayak, S. Nayak, S. Das, S. P. Senanayak and K. Venkatasubbaiah, *Angew. Chem., Int. Ed.*, 2023, **62**, e202216871.
48 P. Nayak, S. Mukherjee, D. Patel, A. A. Mahapatra, A. C. Murali, A. Perumal and K. Venkatasubbaiah, *ACS Appl. Opt. Mater.*, 2024, **2**, 1523–1532.

49 M. Vanga, S. Sa, A. Kumari, A. C. Murali, P. Nayak, R. Das and K. Venkatasubbaiah, *Dalton Trans.*, 2020, **49**, 7737–7746.
50 B. Y.-W. Wong, H.-L. Wong, Y.-C. Wong, M.-Y. Chan and V. W.-W. Yam, *Chem. – Eur. J.*, 2016, **22**, 15095–15106.
51 H. Ye, D. H. Kim, X. Chen, A. S. D. Sandanayaka, J. U. Kim, E. Zaborova, G. Canard, Y. Tsuchiya, E. Y. Choi, J. W. Wu, F. D. R. Fages, J.-L. Bredas, A. D'Aleo, J.-C. Ribierre and C. Adachi, *Chem. Mater.*, 2018, **30**, 6702–6710.
52 M. Yusuf, K. Liu, F. Guo, R. A. Lalancette and F. Jäkle, *Dalton Trans.*, 2016, **45**, 4580–4587.
53 Z. Zhang, H. Zhang, C. Jiao, K. Ye, H. Zhang, J. Zhang and Y. Wang, *Inorg. Chem.*, 2015, **54**, 2652–2659.
54 A. C. Murali, M. Mohanty, R. Singh, I. Mondal, S. Rout, A. Avani, B. K. Patra, S. P. Senanayak and K. Venkatasubbaiah, *Small*, 2025, **21**, e07561–e07561.
55 A. Sahoo, A. Patel, R. A. Lalancette and F. Jäkle, *Angew. Chem.*, 2025, **137**, e202503658.
56 E. J. González, A. M. Sarotti and D. A. Heredia, *Org. Lett.*, 2025, **27**, 8602–8606.
57 J. He, S. Wang, X. F. Song, X. Chang, C. Zou, W. Lu and K. Li, *Chem. Commun.*, 2024, **60**, 11524.
58 J. Full, M. J. Wildervanck, C. Dillmann, S. P. Panchal, D. Volland, F. Full, K. Meerholz and A. Nowak-Król, *Chem. – Eur. J.*, 2023, **29**, e202302808.
59 Y. Zhang, A. Matler, J. Krebs, I. Krummenacher, Q. Ye, H. Braunschweig, T. B. Marder and L. Ji, *Chem. – Eur. J.*, 2024, **31**, e202403973.
60 V. Mukundam, S. Sa, A. Kumari, T. Teja Ponduru, R. Das and K. Venkatasubbaiah, *Chem. – Asian J.*, 2022, **17**, e202200291.
61 P. Nayak, A. Chandrasekar Murali, V. Rao Velpuri, V. Chandrasekhar and K. Venkatasubbaiah, *Adv. Synth. Catal.*, 2023, **365**, 230–237.
62 P. Nayak, A. C. Murali, P. K. Pal, U. D. Priyakumar, V. Chandrasekhar and K. Venkatasubbaiah, *Inorg. Chem.*, 2022, **61**, 14511–14516.
63 P. Nayak, A. C. Murali, V. Chandrasekhar and K. Venkatasubbaiah, *Mater. Adv.*, 2022, **3**, 5893–5899.
64 A. L. Singer and D. A. Atwood, *Inorg. Chim. Acta*, 1998, **277**, 157–162.
65 S. Di Bella, *Dalton Trans.*, 2021, **50**, 6050–6063.
66 A. W. Kleij, *Dalton Trans.*, 2009, 4635–4639.
67 G. Huang, Y. Jiang, J. Wang, Z. Li, B. S. Li and B. Z. Tang, *J. Mater. Chem. C*, 2019, **7**, 12709–12716.
68 J. Miao, Z. Zhang, Z. Cui and M. Zhang, *Mater. Adv.*, 2022, **3**, 2692–2696.
69 Z. Xie, T. Yu, J. Chen, E. Ubba, L. Wang, Z. Mao, T. Su, Y. Zhang, M. P. Aldred and Z. Chi, *Chem. Sci.*, 2018, **9**, 5787–5794.
70 L. Wilbraham, M. Louis, D. Alberga, A. Brosseau, R. Guillot, F. Ito, F. Labat, R. Métivier, C. Allain and I. Ciofini, *Adv. Mater.*, 2018, **30**, 1800817.
71 G. Zhang, J. Lu, M. Sabat and C. L. Fraser, *J. Am. Chem. Soc.*, 2010, **132**, 2160–2162.
72 S. Giannini and J. Blumberger, *Acc. Chem. Res.*, 2022, **55**, 819–830.
73 (*a*) CCDC 2519213: Experimental Crystal Structure Determination, 2026, DOI: 10.5517/ccdc.csd.cc2qkfyp; (*b*) CCDC 2519214: Experimental Crystal Structure Determination, 2026, DOI: 10.5517/ccdc.csd.cc2qkfzq.